Asia-Pacific Journal of Atmospheric Sciences (2022) 58:333–352
https://doi.org/10.1007/s13143-021-00257-y

Online ISSN 1976-7951
Print ISSN 1976-7633

ORIGINAL ARTICLE

Atmospheric Correction of True-Color RGB Imagery with Limb Area-Blending Based on 6S and Satellite Image Enhancement Techniques Using Geo-Kompsat-2A Advanced Meteorological Imager Data

Minsang Kim[1] · Jun-Hyung Heo[2] · Eun-Ha Sohn[2]

Received: 27 April 2021 / Revised: 20 August 2021 / Accepted: 31 August 2021 / Published online: 1 October 2021

Abstract
This study aims for producing high-quality true-color red-green-blue (RGB) imagery that is useful for interpreting various environmental phenomena, particularly for GK2A. Here we deal with an issue that general atmospheric correction methods for RGB imagery might be breakdown at high solar/viewing zenith angle of GK2A due to erroneous atmospheric path lengths. Additionally, there is another issue about the green band of GK2A of which centroid wavelength (510 nm) is different from that of natural green band (555 nm), resulting in the unrealistic RGB imagery. To overcome those weakness of the RGB imagery for GK2A, we apply the second simulation of the satellite signal in the solar spectrum radiative transfer model look-up table with improved information considering altitude of the reflective surface to reduce the exaggerated atmospheric correction, and a blending technique that mixed the true-color imagery before and after atmospheric correction which produced a naturally expressed true-color image. Consequently, the root mean square error decreased by 0.1–0.5 in accordance with the solar and view zenith angles. The green band signal was modified by combining it with a veggie band to form hybrid green which adjust centroid wavelength of approximately 550 nm. The original composite of true-color RGB imagery is dark; therefore, to brighten the imagery, histogram equalization is conducted to flatten the color distribution. High-temporal-resolution true-color imagery from the GK2A AMI have significant potential to provide scientists and forecasters as a tools to visualize the changing Earth and also expected to intuitively understand the atmospheric phenomenon to the general public.

Keywords Atmospheric correction · Look-up table · True-color imagery · Radiative transfer model · Rayleigh scattering · Solar Zenith angle

1 Introduction

Atmospheric radiance is interrupted through absorption, scattering, and diffraction along the atmospheric path. Of these processes, scattering has the most dominant influence in the visible bandwidth and is represented by the Rayleigh scattering effect. The effect of Rayleigh scattering is inversely proportional to wavelength; thus, the blue band—which is the shortest band—is the most affected. As a result, true-color RGB images contain bluish grays (Miller et al. 2016).

To improve the quality of a visible band under the influence of Rayleigh scattering, radiative transfer models (RTMs) have been applied in several studies (Gordon 1993; Rahman and Dedieu 1994; Fukushima et al. 1998; Berka et al. 1999; Richter et al. 2006). RTMs can be used to characterize the atmospheric effects of surface radiation signals as measured by satellite sensors. They have several advantages (He et al. 2019). For instance, they are not limited to a specific region or satellite sensor because they input the atmospheric conditions, geometrical information, and sensory characteristics of areas where the atmospheric

Responsible Editor: Myoung Hwan Ahn.

✉ Jun-Hyung Heo
jhheo89@korea.kr

[1] Korea Ocean Satellite Center, Korea Institute of Ocean Science and Technology, Busan Metropolitan City 49111, Korea

[2] National Meteorological Satellite Center, Korea Meteorological Administration, Jincheon-gun 27803, Korea

correction is to be performed. Moreover, RTM methods are known to be more accurate in simulating atmospheric effects than the empirical line method or improved dark-object subtraction (Zhou et al. 2011).

The second simulation of a satellite signal in the solar spectrum (6S) (Vermote et al. 2006) and moderate resolution atmospheric transmission (MODTRAN) (Adler-Golden et al. 1999) methods have been frequently used in previous research (Richter 1996; Karpouzli and Malthus 2003; Ghulam et al. 2004; Sriwongsitanon et al. 2011; Franch et al. 2013). [emphasize why use 6 S rather than other RTM] However, owing to the complexity of their calculations and consequent large processing times, these RTM methods are inefficient in performing standby calibration over a wide area, such as in the case of satellite imaging. To address this problem, several studies have applied the look-up table (LUT) method; this is an array-based method that replaces runtime calculations with simple array indexing (Liang et al. 2001; Lyapustin et al. 2011; Dorji and Fearns 2018).

A number of previous studies have attempted to estimate surface albedo (the atmospheric reflectance for isotropic light) using various satellite sensors, such as the Advanced Very High Resolution Radiometer (Csiszar and Gutman 1999; Strugnell and Lucht 2001), the Moderate Resolution Imaging Spectroradiometer (MODIS) (Schaaf et al. 2002), and the Spinning Enhanced Visible and InfraRed Imager of the Meteosat (Geiger et al. 2008). Compared to the studies of polar satellites, research into geostationary satellite orbits is sparse; however, recently launched geostationary satellites such as the Geo-Kompsat-2 A (GK2A) Advanced Meteorological Imager (AMI) (Kim et al. 2021), Himawari-8 Advanced Himawari Imager (AHI) (Bessho et al. 2016), Fengyun-4 Advanced Geosynchronous Radiation Imager (AGRI) (Yang et al. 2017), and GOES-16 Advanced Baseline Imager (ABI) (Schmit et al. 2016) are capable of providing higher temporal, spatial, and spectral resolutions. Depending on their sensor, various methods are applied to produce true-color imagery. In the case of AHI, Rayleigh correction is conducted using RTM modified by the National Aeronautics and Space Administration (NASA) SeaDAS and various image enhancement techniques such as hybrid green, and Simple Hybrid Contrast Stretch (SHCS) were applied (Miller et al. 2016). AGRI also applied image enhancement technique SHCS method (Miller et al. 2016). Since the ABI sensor does not have green band, green-like band is generated by combining red, blue, and vegetation band (Bah et al. 2018). They are expected to be used for estimating reflectance, and an increasing amount of research is being undertaken into them.

As described by Vermote et al. (2006), several RTMs mentioned in the previous paragraph are limited because they do not assume a spherical atmosphere; hence, it difficult to apply them to make limb observations (Vermote et al. 2006). In particular, for stationary satellites, the full-disk area covered includes regions at a high solar zenith angle (SZA) of over 70°. In terms of data utilization, accurate surface reflection data are required (Ruddick et al. 2014; Lee et al. 2015). Overcorrection problems occur in several RTMs for polar orbits (Wang 2016) and geostationary satellites (Miller et al. 2016), which commonly assume a flat atmosphere (Adler-Golden et al. 1999; Qu et al. 2003; Vermote et al. 2006). Recently, RTMs have begun to consider the effects of the Earth's curvature as a pseudo-spherical approximation (He et al. 2018). Validation has shown that the model results are comparable to benchmarks (He et al. 2018) showing that the effects of Earth's curvature increase rapidly with SZA, for SZAs of 75°, 80°, and 85°. These results indicate that curvature effects should be considered in high-accuracy atmospheric correction. The Rayleigh scattering LUT has also verified that it shows a significant bias at high SZAs (He et al. 2018).

This study aimed to produce high-quality, true-color RGB images. One important process is that of correcting the sensor-measured radiance of channels affected by Rayleigh scattering through the atmosphere. Rayleigh scattering is dominant within the visible and near-infrared bands; hence, its effects need to be mitigated. We built an LUT that is computed using a 6 S RTM, to convert the radiance to the atmospherically corrected reflectance. Our LUT applies a minimum curvature surface (MCS) technique to augment the LUT in terms of geometric parameters. Inspection of the resulting LUT shows that the atmospheric correction coefficients dramatically increase over SZAs and view zenith angles (VZAs) of 70°. This caused the reflectance near the limb area exceeds the correction values. To mitigate this reflectance, we applied limb correction according to the SZA and VZA. The GK2A AMI, which has a visual area specification similar to that of the AHI sensor in Himawari-8, contains a green band centered at 510 nm. The band is slightly shifted toward the blue band compared to the 550 nm found in many other sensors (MODIS, Landsat, and VIIRS) (Miller et al. 2016; Broomhall et al. 2019). For this reason, the vegetation in the true-color RGB images is browner and the bare ground is redder than that of the aforementioned sensors. One solution to this problem is hybrid-green adjustment, which combines the green visible band with the near-infrared band (870 nm) to mimic green grass vegetation. We applied hybrid green instead of the original green band. True-color RGB imagery incorporating atmospheric correction shows up dark. One remedial method is histogram equalization. This method brightens the image by expanding the narrow color distribution. True-color RGB imagery is useful in detection and analysis.

In this paper, we describe the atmosphere-corrected, true-color RGB imaging procedure from GK2A AMI. Section 2 describes the data used in this study and the methodology for

obtaining the atmospherically corrected visible bands and image enhancements. The preliminary results of applying each process—along with their respective final products—are described in Section 3. Section 4 discusses the limitations and future works. The paper is concluded in Section 5.

2 Data and Methodology

2.1 Data

2.1.1 GK2A AMI

GEO-KOMPSAT-2 A is a geostationary meteorological satellite that was launched on December 5, 2018 and began operation on July 24, 2019. It was designed to take over the meteorological functions of the Communication, Ocean, and Meteorological Satellite (COMS), performing meteorological and space-weather observation tasks using the AMI. The AMI exhibits a superior observational performance to the COMS in terms of spatial, temporal, and spectral resolutions (Kim et al. 2021).

In particular, the augmented array of channels—the number of available channels was expanded from five to 16—has led to the improvement of satellite measurement capacities (Table 1). The composite of red, green, and blue visible light channels enable true-color imagery; this represents a milestone improvement over the gray-color imagery previously available. Three water-vapor channels facilitate the detection of water-vapor signals at different heights, and the various infrared channels detect atmospheric gases and subtle changes in convective signals.

Spatial and temporal resolutions were also enhanced. The red channel has a resolution of 0.5 km, the two other visible channels and the 860 nm channel have a resolution of 1 km, and the infrared channels have 2 km spatial resolution. The observation cycle of the AMI has a duration of 10 min for the full disk and 2 min for the Korean Peninsula region. Its payload covers a full disk area centered at 0°N, 128.3°E; this includes Asia and Oceania, which contain various land-cover types and diverse climate phenomena.

Table 2 compares the full width at half-maximum (FWHM) responses and the spatial resolutions of GEO (AMI, AHI, AGRI, and ABI) sensors for specific bands of focus. There is only a subtle difference between AMI and AHI, because they use the same sensor (Bessho et al. 2016). AGRI and ABI has no green band, which means that it must take advantage of near-band values to obtain imaginary green values (Schmit et al. 2016). On the other hand, the AMI and AHI feature a green band; however, this signal is slightly blue-shifted, which results in another imaginary green value, referred to as "hybrid green" (Miller et al. 2016). Outside of the visible range, the AMI features a cirrus band (1.4 μm); however, the cloud particle size band (2.2 μm) is absent. Both are included in the AHI and ABI.

Table 1 GEO-KOMPSAT-2 A channel specifications, center of wavelength, bandwidth, and resolution (Kim et al. 2021)

GK2A channel specification	GK2A band #	Center of wavelength (μm)	Bandwidth (μm)	Resolution (km)
Visible	1	0.47	0.43–0.48	1
	2	0.51	0.50–0.52	1
	3	0.64	0.63–0.66	0.5
Near Infrared	4	0.86	0.85–0.87	1
	5	1.37	1.37–1.38	2
	6	1.61	1.60–1.62	2
Water Vapor	7	3.83	3.74–3.96	2
	8	6.2	6.06–6.42	2
	9	6.9	6.89–7.01	2
Infrared	10	7.3	7.26–7.43	2
	11	8.6	8.44–8.76	2
	12	9.6	9.54–9.72	2
	13	10.4	10.25–10.61	2
	14	11.2	11.08–11.32	2
	15	12.3	12.15–12.45	2
	16	13.3	13.21–13.39	2

Table 2 Comparison of the GEO-KOMPSAT-2 A advanced meteorological imager (AMI) (Kim et al. 2021), Himwari-8 advanced Himawari imager (AHI) (Bessho et al. 2016), Advanced Geosynchronous Radiation Imager (AGRI) (Yang et al. 2017), and GOES-R advanced baseline imager (ABI) (Schmit et al. 2016) sensor in full width at half-maximum (FWHM), and spatial resolution at nadir for selected visible and near-infrared bands

Sensor	AMI			AHI			AGRI			ABI		
	No.	FWHM(μm)	Res. (km)	No.	FWHM(μm)	Res. (km)	No.	FWHM (μm)	Res. (km)	No.	FWHM (μm)	Res. (km)
Blue	1	0.43–0.48	1.0	1	0.43–-0.48	1.0	1	0.45–0.49	1.0	1	0.45–-0.49	1.0
Green	2	0.50–0.52	1.0	2	0.50–0.52	1.0	-	-	-	-	-	-
Red	3	0.63–0.66	0.5	3	0.63–0.66	0.5	2	0.55–0.75	0.5	2	0.59–0.69	0.5
Vege.	4	0.85–0.87	1.0	4	0.85–0.87	1.0	3	0.75–0.90	1.0	3	0.85–0.89	1.0

2.1.2 ECMWF CAMS Near-real-time Data

The European Centre for Medium-Range Weather Forecasts (ECMWF) has produced the Copernicus Atmosphere Monitoring Service (CAMS) dataset. CAMS also offers an atmospheric analysis service, which focuses on atmospheric composition, including aerosols, chemical species, and greenhouse gases (Massart et al. 2016; Inness et al. 2019). The CAMS analysis is produced using the ECMWF's four-dimensional variational (4DVar) system (Engelen and McNally 2005) within the Integrated Forecasting System (IFS; version CY42r1 for 2016 and CY43r1 for 2017), which is one of the world's leading operational global weather-prediction systems. The transport of tracers such as CO_2 is assessed online by the IFS model concurrently with the meteorological forecast. Because the semi-Lagrangian advection scheme in the IFS does not conserve mass, a global mass fixer is applied to restore mass conservation to the global budget (Agust-Panareda et al. 2014). The IFS model used in CAMS has a horizontal resolution of approximately 40 km and 137 vertical levels. Further information about the IFS model can be found online (https://www.ecmwf.int/en/forecasts/documentation-and-support/changes-ecmwf-model/ifs-documentation). The forecast contains information pertaining to gases in the lowest layer of the atmosphere (troposphere) and the ozone higher up (stratosphere). It also contains data about desert dust, sea salt, organic matter, black carbon, and sulfate particles (aerosols). The initial conditions of the forecasts (analyses) are obtained by combining a previous forecast with satellite observations of the aerosol, ozone, carbon monoxide, nitrogen dioxide, and sulfur dioxide levels, via a process called data assimilation. In this study, we used a three-parameter geostationary environmental monitoring spectrometer, which measures six-hourly instantaneous values of the total column ozone (TCO), total column water vapor (TPW), and total aerosol optical depth (AOD) at 550 nm from the CAMS dataset, interpolating them onto a 0.25° longitude × 0.25° latitude grid (Table 3). This dataset was re-projected to the GK2A full-disk region.

Table 3 European Centre for Medium-Range Weather Forecasts (ECMWF) Copernicus Atmosphere Monitoring Service (CAMS) data characteristics

Parameters [unit]	Spatial resolution (km)	Temporal resolution
Total column ozone [atm − cm]	12.5	Daily
Total precipitable water [gcm^{-2}]	12.5	Daily
Aerosol optical depth at 550 nm	12.5	Daily

2.2 Methodology

Figure 1 illustrates the procedure of atmospherically correcting true-color imagery. The sensor-measured reflectance is reduced by atmospheric scattering. The Rayleigh scattering effect is inversely proportional to wavelength, thus visible channels needed to be corrected accordingly. Without reduction, we constructed an LUT by considering geometric and atmospheric conditions, using the 6 S RTM to correct atmospheric effects in visible channels.

Inspection of the created LUT showed that the atmospheric correction coefficients were dramatically increased over 70° of SZA and VZA (Miller et al. 2016). As a result, the reflectance near the limb area exceeded the correction values. To mitigate reflectance, we applied limb correction according to the SZA and VZA.

The GK-2 A green-channel wavelength (510 nm) differs from the green grass vegetation wavelength (550 nm) taken from the spectral database of NASA's Advanced Spaceborne Thermal Emission and Reflection Radiometer. One solution is the hybrid-green method, which combines the visible light band with the near-infrared band (870 nm) to mimic green grass vegetation. We applied hybrid green instead of the original green band.

True-color RGB imagery incorporating atmospheric correction shows up dark. One remedial method is histogram equalization. This method aims to increase the brightness of the image by expanding the narrow color distribution. True-color RGB imagery is useful for detection and analysis.

2.2.1 6SV2.1

The 6S is a basic RTM; it has been used for the calculation of LUTs in the satellite atmospheric correction algorithms developed by Vermote et al. (2006). It is designed to simulate the reflection of solar radiation from the atmosphere–surface coupling system over a wide range of air, spectrum, and geometric conditions. This enables accurate simulation of satellite observations, consideration of the elevated targets, and modeling of the composite atmosphere of realistic molecules and aerosols. 6S is a highly accurate radiative transfer model considering wide range of atmospheric conditions. Compared with Simplified Method for the Atmospheric Correction (SMAC), 6S showed better performance [Proud et al. 2010]. The latest updates include a public release of its vector version (6SV), which considers the Stoke's parameter and polarization contribution; this version is based on the successive orders of scattering (SOS) approximations. The accuracy of radiative transfer (RT) calculations can be varied by changing the number of calculation angles and parameters (Vermote et al. 2006). The 6S model atmosphere consists of several layers, and the model solves the RT equations

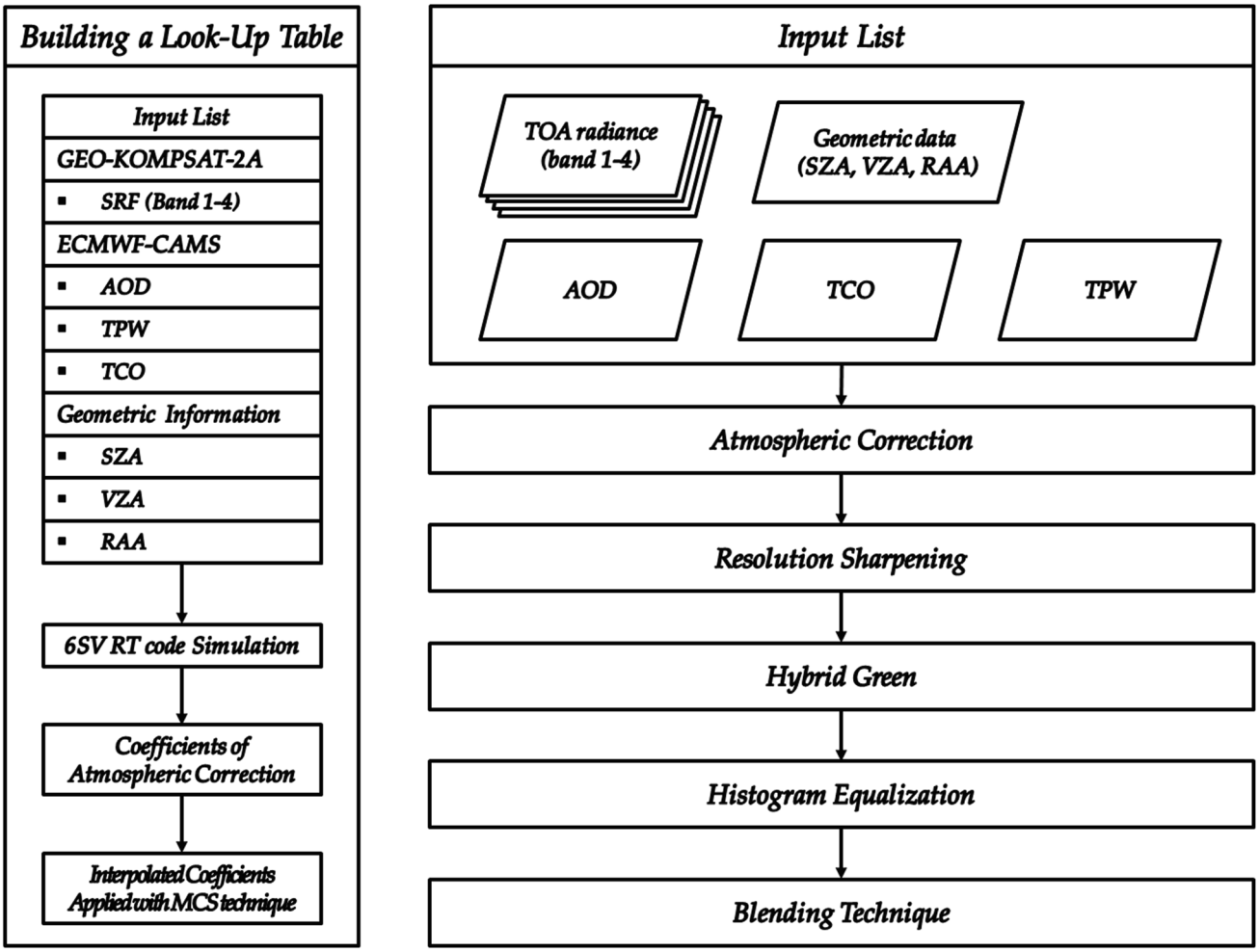

Fig. 1 Flowchart of the atmospheric correction process for true-color imagery

numerically, layer by layer. The final result is a sum of successive computations, which is performed by integrating over the Fourier series decomposition. Unlike other RT codes, the 6S offers an innovative working system. The 6SV calculates surface reflectivity, not remote sensing reflectance—which is total surface incident irradiance (downward irradiance) divided by aquatic luminance. In the calculation, the apparent reflectance value is arbitrarily set (assuming 0, 0.5, 1.0 in the model) and the radiance is inversely calculated. In this process, the 6S model generates the atmospheric background, returning transmittance, and top of atmosphere (TOA) reflectance. It provides correction coefficients to compute the ground reflectance, given a TOA radiance. It was publicly released in May 2005, and the latest version of the 6SV code (6SV2.1), released in June 2015, is now available for download: http://6s.ltdri.org/pages/downloads.html.

The land surface reflectance in the 6SV atmospheric correction mode is calculated using the following equation:

$$\rho_{\mathrm{TOA}}(\theta_s, \theta_v, \varphi) = T_g(\theta_s, \theta_v) \times \left[\rho_{R+V} + T^{\downarrow}(\theta_s) T^{\uparrow}(\theta_v) \frac{\rho_s}{1 - S\rho_s}\right] \quad (1)$$

with

$$\rho_s = \frac{\frac{\rho_{\mathrm{TOA}}(\theta_s, \theta_v, \varphi)}{T_g(\theta_s, \theta_v)} - \rho_{R+V}}{T^{\downarrow}(\theta_s) T^{\uparrow}(\theta_v)} \quad (2)$$

where ρ_{TOA} is the TOA reflectance; θ_s is the SZA; θ_v is the VZA; φ is the relative azimuth angle (RAA); T_g is the gaseous transmission of atmospheric gases such as H2O, CO2, and O3; ρ_{R+V} is the total reflectance due to molecular and aerosol scattering; $T^{\downarrow}(\theta_s)$ and $T^{\uparrow}(\theta_v)$represent the atmospheric transmittance from sun to target and target to satellite, respectively; and ρ_s is the atmospheric reflectance for a Lambertian, homogeneous target. The 6SV computes all transmittance and atmospheric reflectance using the user-defined parameters and subroutines, which contain vertical profiles of atmospheric temperature, pressure, and absorbing gases

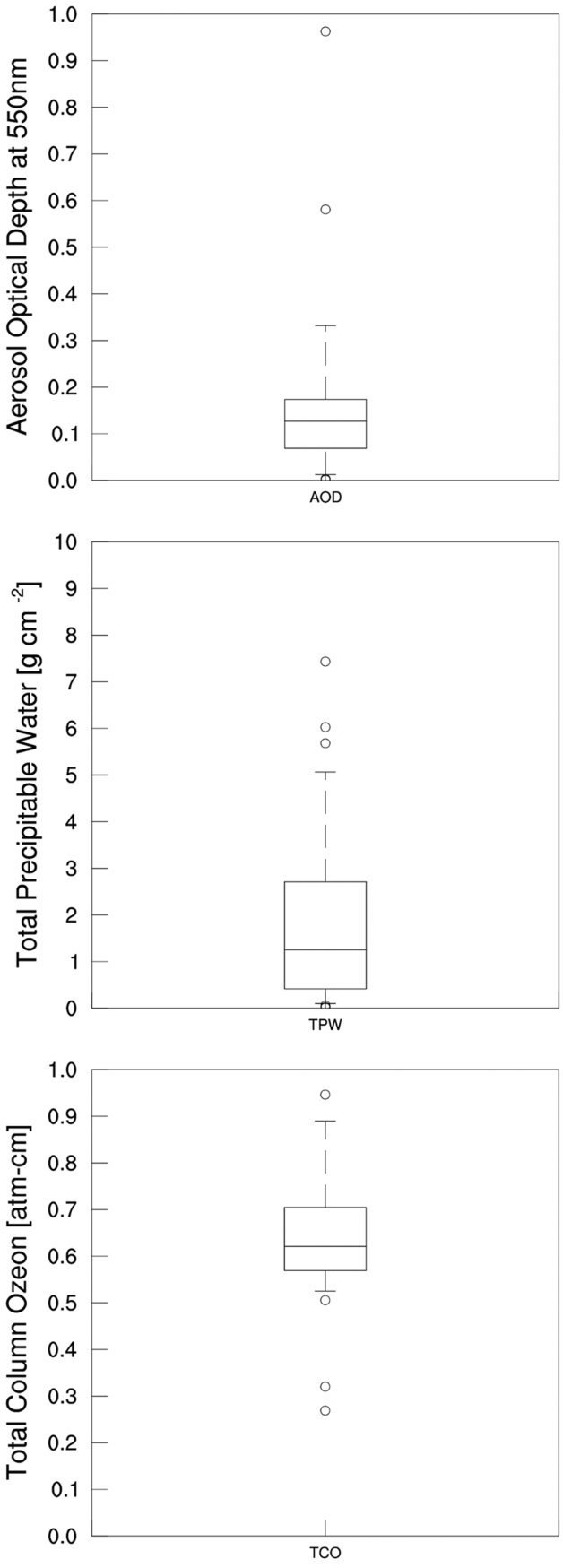

Fig. 2 Range and intervals of atmospheric conditions, selected based on the climatology of the ECMWF CAMS data from 2015 to 2018 ▶

according to altitude. This model provides three atmospheric correction coefficients for removing atmospheric effects. The land surface reflectance can be calculated using Eq. (3) with the atmospheric correction coefficients:

$$\rho_{\text{atm}} = \frac{x_a \times L - x_b}{1 + x_c \times (x_a \times L - x_b)} \tag{3}$$

where ρ_{atm} is the atmospherically corrected reflectance; L is the TOA radiance [$\text{Wm}^{-2}\mu m^{-1}sr^{-1}$]; and x_a, x_b, and x_c are atmospheric correction coefficients which represent the inverse of the transmittance, the scattering term of the atmosphere, and the spherical albedo, respectively.

2.2.2 Building a 6SV2.1 LUT

The 6SV was developed specifically to determine atmospheric corrections for satellite, it allows users to define a down-looking geometry. Despite the direct atmospheric corrections of reflectance available with 6S, most studies have performed atmospheric corrections using LUT approaches. Using a LUT can prevent duplicate calculations for identical conditions in limited computational environments.

First, for building our LUT, input parameters were set using the following preconditions described in Table 4. For geometric conditions, each SZA and VZA was set between 0° and 80°, in increments of 5°. The RAA had a range from 0° to 180°, in increments of 10°. The range and intervals of atmospheric conditions were selected based on climatology of the ECMWF CAMS data from 2015 to 2018 (Fig. 2). The TCO had a range of 0.25–0.40 atm-cm and was varied in 0.05 atm-cm increments. TPW had a range of 0–5 gcm^{-2}, and was varied in 1 gcm^{-2}increments. The AOD had a range of 0.01–0.3, with irregular intervals. The reflectance height was segmented between ground level and a height of 10 km, in 2 km intervals. The spectral conditions were configured using the spectral response function of GK2A.

The three pre-calculated atmospheric correction coefficients were stored in the LUT. To expand the LUT, an MCS technique was applied. The MCS is a mathematical method for constructing smooth surfaces from irregularly spaced data. The surface of minimum curvature corresponds to the minimum of the Laplacian power or—in the alternative formulation—satisfies the bi-harmonic differential equation. Physically, it models the behavior of an elastic plate. In the one-dimensional case, the minimum curvature leads to the natural cubic spline interpolation. In the two-dimensional case, a surface can be interpolated with bi-harmonic splines or gridded with an iterative finite-difference scheme (Smith and Wessel 1990). In most practical cases, the minimum

Table 4 Configuration of second simulation of a satellite signal in the solar spectrum (6S) interpolated look-up table (LUT)

Parameters [unit]	Min	Max	Number of segments (interval)
Solar zenith angle [°]	0	70	15 (5)
View zenith angle [°]	0	70	15 (5)
Relative azimuth angle [°]	0	180	19 (10)
Total column ozone [atm − cm]	0.25	0.40	4 (0.05)
Total precipitable water [gcm^{-2}]	0	5	6 (1)
Aerosol optical depth at 550 nm	0.01, 0.05, 0.1, 0.2, 0.3		5
Reflectance height [km]	0	10	6 (2)

curvature technique produces a clear, smooth surface (Rabah and Kaloop 2013). In this study, it was assumed that the atmospheric correction coefficients would change smoothly in response to the SZA and VZA when all other conditions are held constant. The SZA and VZA are specified starting from 5° with an interval of 0.5° in the final version of the LUT.

After atmospheric correction of the reflectance, the composite true-color imagery featured a particular limb region highlighted in red, whereas the uncorrected true-color imagery did not. The red coloration was a result of the blue and green bands used in the RGB composite being overcorrected with respect to the red band. The 6S was designed using a parallel-plane atmosphere assumption in the RT model (which reduces the Rayleigh scattering effect), and the impact was exaggerated at high zenith angles, such that the Earth's limb appeared red. It is possible to mitigate overcorrection at the limb by reducing the Rayleigh scattering according to the atmospheric pathlengths and storing the level of reflectance in the LUT. RT codes set reflectance points at ground level. Additional height levels were added into the LUT, and the height indexes were defined as in the Table 5.

The purpose of cloud height index is to reduce excessive Rayleigh scattering as the optical distance increases at high zenith angle, assuming an altitude of reflective surface. To estimate altitude of reflective surface, the brightness temperature value of the infrared channel was used since the altitude at which radiation occurs can be inferred from the temperature of the radiation surface. It is applied all regions regardless of latitudes and atmospheric states.

Table 5 Reflectance height level and range of brightness temperature corresponding to height index

Height index	Reflectance height level	Range of brightness temperature (BT)
0	Ground level (0 km)	$BT \geq 260$ K
1	2 km	$260\ K > BT \geq 250$ K
2	4 km	$250\ K > BT \geq 240$ K
3	6 km	$240\ K > BT \geq 230$ K
4	8 km	$230\ K > BT \geq 220$ K
5	10 km	$220\ K > BT$

2.2.3 Image Processing

A difference in spatial resolution occurs when multi-band datasets are generated from different bands. The 640 nm band has the highest spatial resolution (about 500 m), other visible channels and vegetation channels have a 1 km spatial resolution, and infrared channels have a 2 km spatial resolution. To compose true-color imagery, each band is required to have equal spatial resolution; thus, all bands (except the 640 nm band) were downscaled to a 500 m spatial resolution. Spline interpolation—a statistical downscaling method—was used to sharpen resolution; it is a form of interpolation in which the interpolant is a special kind of piecewise polynomial, called a spline. The spline interpolation is preferred over polynomial interpolations because the interpolation errors can be reduced, even when using low-degree polynomials for the spline. Spline interpolation avoids the problem of Runge's phenomenon, in which oscillations occur between points when interpolating with high-degree polynomials.

The uncorrected true-color imagery results in brown vegetation and red bare soil (Fig. 3). The explanation for these unexpected colors is that the signal center of the green

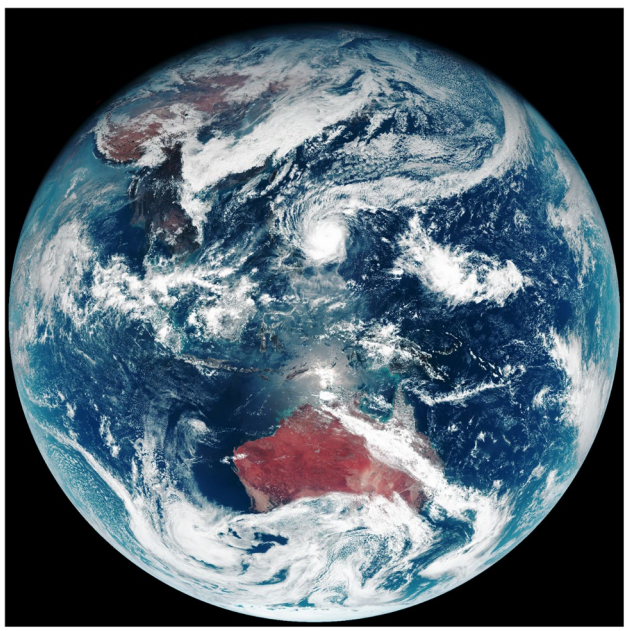

Fig. 3 Step 1: GK-2 A full-disk simple composite of native RGB-band true-color image, taken on 2019/12/01 0300 UTC

band (510 nm) in the AMI sensor is slightly blue-shifted compared with that of other sensors (MODIS, VIIRS, etc.), which are centered at 550 nm for the green band. Subtle differences produce color changes in true-color imagery, as described by Miller et al. (2016).

To correct this unrealistic green color, Miller et al. (2016) suggested a hybrid green, which is a composite of the original green band and a vegetation band that is sensitive to chlorophyll signals—this is used to monitor vegetation health. The hybrid green is calculated using the following equation:

$$Hybrid\ green = R_{green} \times \left(1 - F_{hg}\right) + R_{vege} \times F_{hg} \quad (4)$$

where F_{hg} is the hybrid-green factor (which varies from zero to one; in this study, the hybrid-green factor was set to 0.13 empirically), and R_{green} and R_{vege} are the reflectances of the green and vegetation bands, respectively. The hybrid-green factor adjusts the vegetation signal, highlighting green colors and faded red soil. The use of the vegetation band is not appropriate for the surface of oceans because of the strong absorption by water of light in those wavelengths. However, an ocean is relatively sensitive to the blue band and the practical effect of using the hybrid-green method in true-color imagery is more pronounced.

The original true-color composite imagery appears faint unless color distributions are enhanced. To compensate for indistinguishable imagery, the visual enhancement technique of histogram equalization was implemented. Histogram equalization is an image-processing technique designed to improve contrasts in images by redistributing the color histogram. A well-separated image has advantages in terms of visibility and sharpness, particularly over blurred or dark images. Histogram equalization method brightens the image by expanding the narrow color distribution. Through this adjustment, the intensities can be better distributed on the histogram utilizing the full range of intensities evenly. This allows for areas of lower local contrast to gain a higher contrast. Histogram equalization accomplishes this by effectively spreading out the highly populated intensity values which use to degrade image contrast. First, reflectance values (0–1) were rescaled to between zero and 255, because the RGB composite imagery contained pixel values within this range. These rescaled reflectance values were used to compute the cumulative density function (CDF). The last process was to convert the reflectance values by multiplying them with respect to the CDF of each intensity.

The pixel values at high SZA or VZA can become very large and unrealistic, owing to overcorrection by the 6S RTM. Because the correction breaks down nonlinearly for very long atmospheric pathlengths near the Earth's limb, the corrected imagery features a reddening edge (Miller et al. 2016). Using the uncorrected reflectance datasets, we performed data-blending at the extremities of the SZA and VZA, to remove this reddening edge and achieve true-color imagery after the atmospheric correction process. The corrected reflectance data were blended gradually according to the zenith angles, becoming less corrected toward the edge of the limb. The blending factor was calculated in terms of the SZA and VZA, it was linearly decreased from 1.0 to 0.0 over zenith angles from 75° to 90° and 65° to 85°, respectively.

3 Results

3.1 Preprocessing For Atmospheric Correction of TOA Reflectance

Rayleigh scattering exerts a dominant effect along atmospheric pathways and is an important feature of visible channels. It is inversely proportional to the fourth power of the wavelength. The upper images in Fig. 4 are uncorrected, and they all exhibit the Rayleigh effect. The blurred regions, when compared with the lower images in the figure, indicate that the surface reflectance suffered Rayleigh scattering before the signal reached the satellite. The edges of Earth (which become more pronounced moving from the red to blue columns) experience a larger scattering effect because the longer the optical pathlength from the target to the satellite along the atmospheric path, the greater the Rayleigh scattering effect. Atmospherically corrected imagery, which adjusts for the Rayleigh scattering effects, can achieves the clearer earth imagery exemplified in the lower images of Fig. 4.

Figure 5 shows an example of atmospherically corrected GK-2 A full-disk true-color RGB imagery; it indicates that the adjustment for Rayleigh scattering removes much of the atmospheric haze, yields sharper contrasts between the cloud and surface features, and enhances the overall surface detail. Despite the atmospheric corrections, red regions remain present where the atmospheric pathlength is long. This is a result of overcorrection; clouds and aerosols at high zenith angles exert an influence on the visible channel, depending on their height and opacity. The Rayleigh correction does not account for these clouds and aerosols; instead, it assumes a 6S RTM. To resolve this problem, Section 3.2 describes how the LUT factors in target elevation when calculating TOA reflectance.

The reddening of Earth's limb is a result of overcorrection in the green and blue bands. This is consistent with the results of Lee et al. (2015), who found that the atmospheric correction-coefficient values computed in 6S were dramatically increased above a 60° zenith angle. This may be due to limitations of the RT code at high angles, and these limitations are difficult to quantify without the corresponding

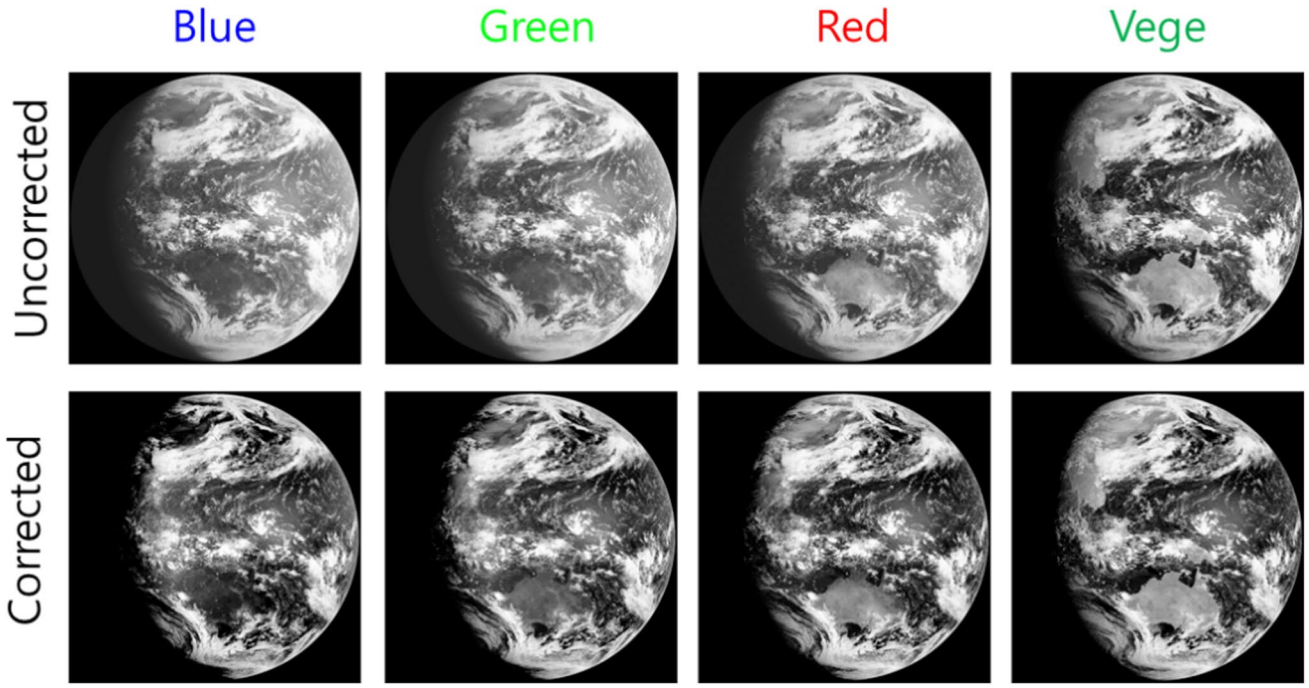

Fig. 4 Effect of atmospheric correction on the GK-2 A full-disk visible-band imagery. Upper images represent uncorrected band imagery and lower images represent corrected band imagery

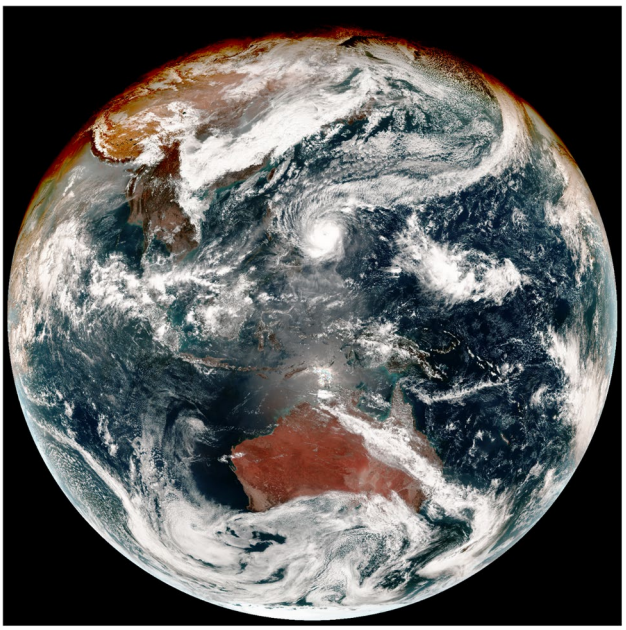

Fig. 5 Step 2: example of atmospherically corrected GK-2 A full-disk true-color RGB imagery, same date with Fig. 3

in situ measurements. It may be possible to improve the correction at the limb by reducing the angular increment in the LUT (Broomhall et al. 2019). Figure 6 shows the effects of correcting for atmospheric pathlength by considering target elevation in the LUT. By computing target elevation separately and using them in atmospheric pathlength corrections, the reddening of the Earth's limb can be reduced. The 10.4-μm BT used to estimate the reflecting surface height is only approximate; however, the results show that atmospheric correction is improved at high zenith angles.

3.2 Image Processing

Figure 7 shows the effects of attenuation in green true-color on the Australia region. The native true-color imagery exaggerates the reddish soil and dark grass; this is because the vegetation has a peak reflectance of around 550 nm due to the presence of chlorophyll, which is why most of the other sensors' green bands target this peak (Broomhall et al. 2019). However, the true-color imagery supplemented by hybrid-green color showed more realistic vegetation and a brown soil color. The true-color image applied with hybrid green in Fig. 7 is similar to the MODIS Terra Rayleigh-corrected RGB images with its 555 nm green band. Several other works using the Himawari-8 AHI true-color RGB images applied with hybrid green (Miller et al. 2016; Broomhall et al. 2019) are also consistent with the result from GK2A .

Figure 8 shows the result of applying histogram equalization to a Rayleigh-corrected, hybrid green-applied true-color RGB image. The original image on the left-hand side is dim and has poor contrast, whereas the right-hand image is brighter and has better contrast (Fig. 8). The color distributions of R, G, and B before histogram equalization

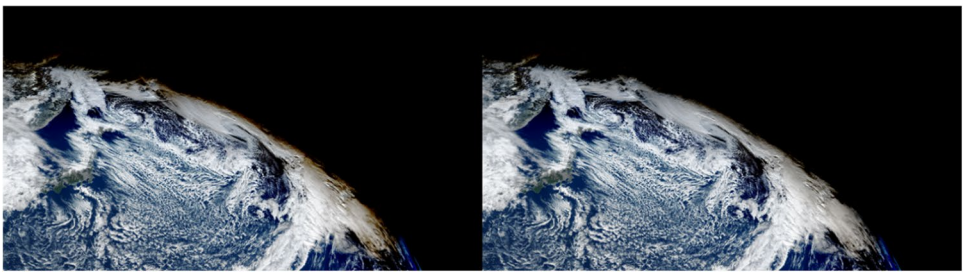

Fig. 6 Step 3: effect of altitude assignment in look-up table (LUT): (**a**) fixed at ground level, and (**b**) applied height using IR brightness temperature (BT) of 10.4 μm

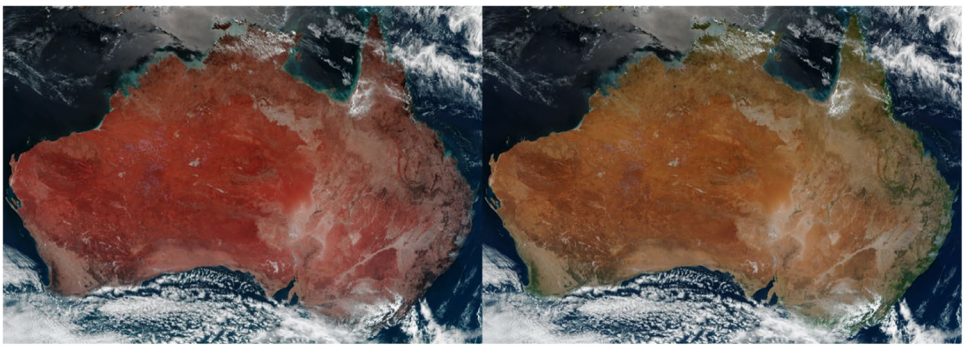

Fig. 7 Step 4: comparison of GK-2 A using (**a**) simple composite of native RGB and (**b**) hybrid RGB on Australia, taken on 2019/11/06 0300 UTC

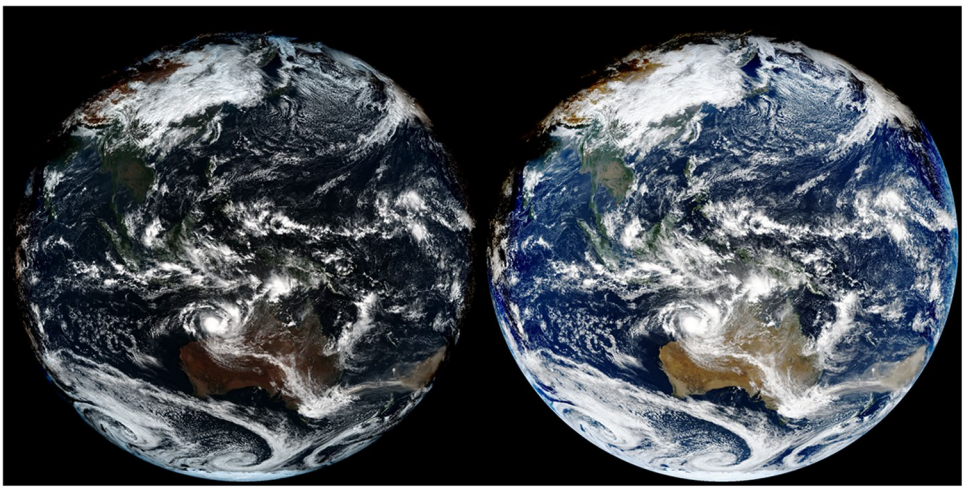

Fig. 8 Step 5: comparison of GK-2 A using (**a**) atmospherically corrected true-color RGB and (**b**) atmospherically corrected and enhanced true-color RGB imagery taken on 2020/01/06 0100 UTC

were narrow, with each color having a different center (not shown). With histogram equalization applied, the color distribution becomes uniform, this method is effective in improving the visual appearance of dark images. As a result, the difficulties of distinguishing between cloud surfaces and the ocean are alleviated, and the characteristics of various surface types can be visualized. Moreover, for clouds (which are highly reflective areas), a more detailed representation is possible, thereby improving the utility of this imagery for assessing cloud textures.

In Fig. 9, the atmospherically corrected true-color RGB imagery is blended with uncorrected imagery near the limb. The uncorrected AMI data are more consistent for the Earth's limb in comparison to the MODIS imagery; however, in the Rayleigh scattering-corrected true-color imagery, errors increase exponentially along long optical trajectories through the atmosphere. In the blending stage of our proposed procedure, the proportion is varied linearly from 100 to 0 % for SZAs between 80° and 90°. Most edge effects that had not been removed by the previous pathlength corrections were reduced. The procedure also resulted in a more realistic transition between Earth and space than the atmospherically corrected true-color RGB imagery. Figure 9 presents the final true-color image, in which all of the aforementioned techniques have been applied.

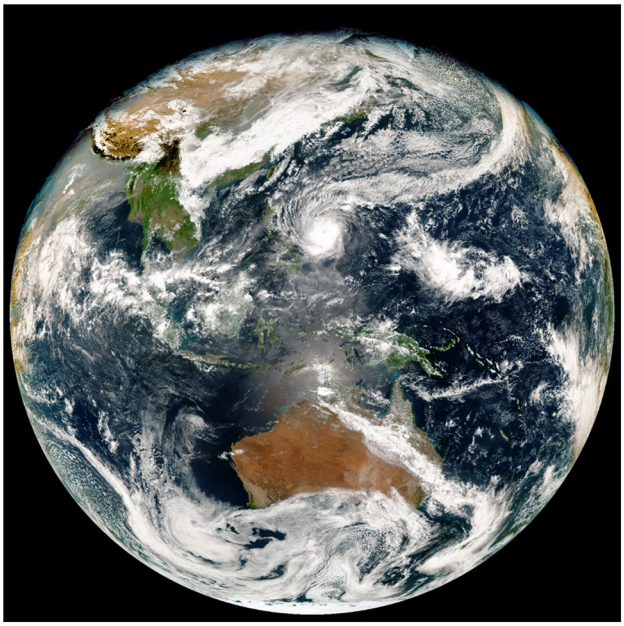

Fig. 9 Final step: final true-color imagery applying all the aforementioned techniques same date with Fig. 3

3.3 Robust Result for Atmospheric correction of GK2A visible bands

To obtain robust results for atmospheric correction of the GK2A visible band with visual true-color RGB inspection, we quantitatively examined the results of atmospheric correction based on 6S LUT along with various SZA and VZA conditions. Figure 10(a) and (b) show an example image of the spatial distribution of SZA and VZA at 2020.07.07 03 UTC. Because a geostationary satellite is situated in a fixed location, VZA does not change with time. However, in the case of SZA, it changes greatly depending on the season or time; therefore, in this study, we used the reflectance of 03 UTC in the four seasons. We sampled approximately 121 million pixels per image on four channels of GK2A. Figure 10(c) and (d) show the SZA and VZA distributions of the sampled pixels for quantitative evaluation of reflectance. The distributions are non-uniform for both SZA and VZA. The majority of the samples exist around 40 degrees and the number of samples decreases with distance away from the peak degrees.

Figure 11 shows the averaged root mean square error (RMSE) of the difference between the original and atmospheric-corrected reflectance (blue) and difference between the original and blended reflectance after atmospheric correction (red) as a function of SZA for each band per season. Although there are slight differences depending on the season, the reflectance RMSE range for all sampled data is 0–0.5. In general, the RMSE due to atmospheric correction increases with the SZA. In particular, the RMSE increases sharply as it exceeds 70 degrees. This is because the scattering effect of the original band becomes stronger as the SZA increases. The RMSE of the reflectance difference due to atmospheric correction becomes more noticeable with the transition from the red channel to the blue channel. This result is consistent with the stronger scattering effect toward the blue channel.

Blending is a method designed to improve images in areas with SZA greater than 70 degrees, which not only mitigates red areas due to atmospheric over correction at high zenith angle, but also helps with natural representation. As a result, Fig. 11 shows the effect of blending process that reduces the rapid increase in RMSE when only atmospheric correction is applied. Similar to the application of atmospheric correction effect, the variability according to the season is not large, and the scattering effect increases as the channel wavelength decreases, hence RMSE increases.

Figure 12 shows the averaged RMSE of the difference between the original and atmospheric-corrected reflectance (blue) and difference between the original and blended reflectance after atmospheric correction (red) as a function of VZA. The improvement by atmospheric correction becomes more noticeable as VZA increases. The reason is that the longer the optical path is, the more pronounced is the effect caused by the atmosphere. The improvement effect increases with the blue band. In VZA, the effect of the reduction due to blending varies from band to band and season to season, but it reduces RMSE, as a result, helps improve the quality of images. The averaged RMSE (observation-based reflectivity-atmospheric-corrected reflectance, and atmospheric-corrected reflectance-blended reflectance) shows the improvement of the true-color RGB imagery. Although the improvement due to atmospheric correction is not applied in all areas and therefore, the blending technique is applied at high angles, the reflectance error due to the Rayleigh scattering is improved. As a result, clear results can be obtained in the actual image.

3.4 Illustrative Examples

True-color imagery is designed to represent Earth in a manner similar to how normal human color vision represents it. This real-color imagery helps in identifying surface types (e.g., land, ocean, ice, and snow) and atmospheric properties such as cloud, fog, dust, and ash; it produces important information by condensing three bands into one image, with the advantage of allowing easy communication of this information. Therefore, it is useful in enabling people to intuitively interpret weather phenomena without special training, and it can be very helpful to both forecasters and the general public.

There are several examples of true-color RGB imagery being employed to consider weather events. In satellite

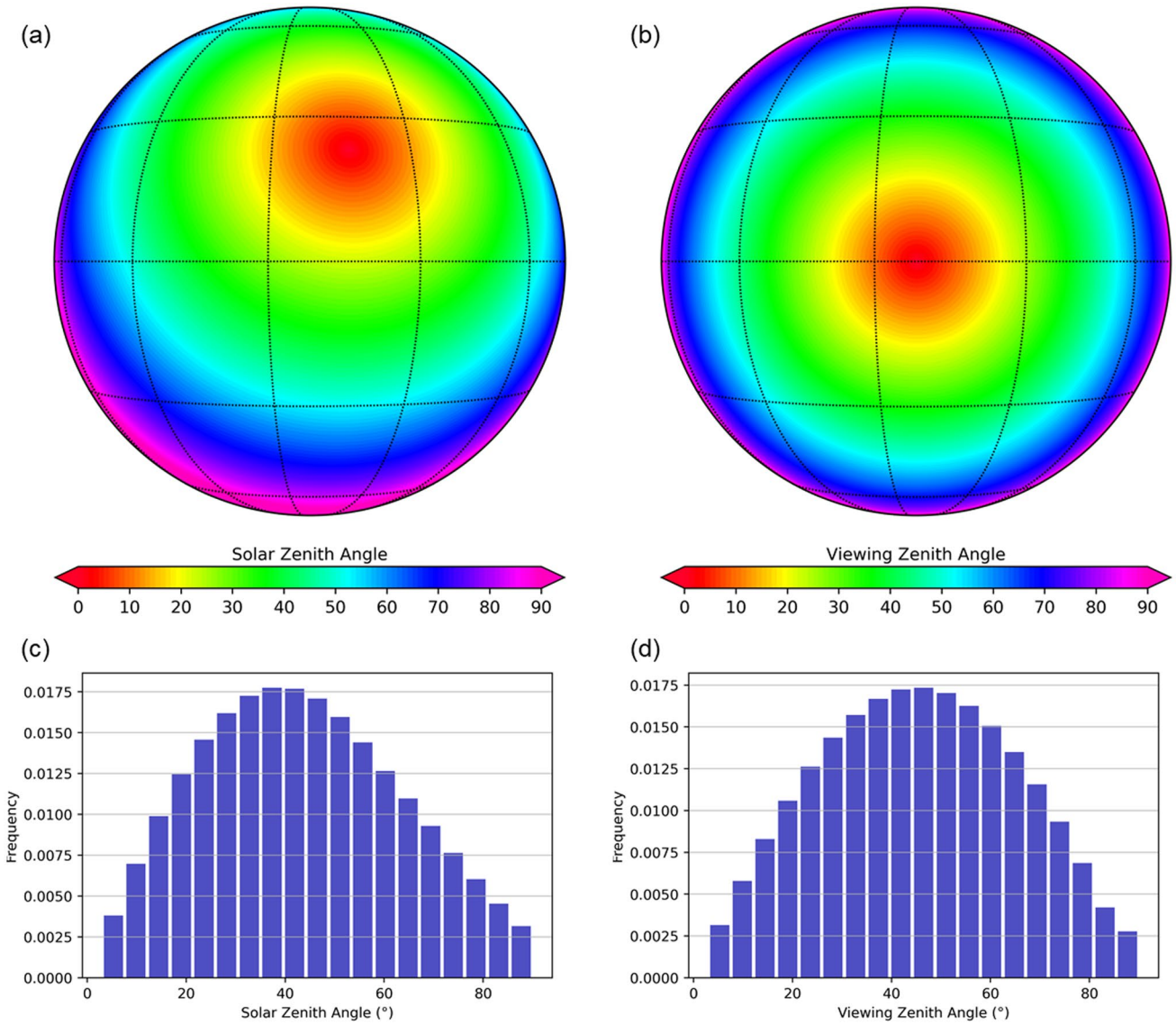

Fig. 10 Spatial distribution of (**a**) SZA and (**b**) VZA at 2020.07.07 03 UTC. Histogram of (**c**) SZA and (**d**) VZA of sample pixels

observation, the texture of fog is flat and edges of the clouds are sharp. Nevertheless, the cloud environments at low levels cannot be evaluated because the satellite detects energy from reflecting or radiating surfaces. For the same reason, fog is difficult to distinguish from low cloud, because they both generate optically thick and warm cloud textures. GK2A RGB fog imagery is used to detect fog and low-level cloud. This imagery uses different composites of red, green, and blue channels for day and night; however, fog and low cloud are colored as cyan. One method of distinguishing fog from low cloud is that of animating cloud patterns. The movement of fog is relatively slow compared with that of low cloud, and the surface texture of fog is flat. Figure 13 shows an example of true-color and RGB fog images taken of the Korean Peninsula. The fog and lower clouds are located at the West Sea and the Liaodong Peninsula; they are distinguishable from the high, thick clouds over the Shandong Peninsula (red box). However, it is difficult to discriminate low-level cloud using the GK2A fog imagery, because they are represented by similar colors and shapes. In the true-color RGB imagery, they have different external cloud surfaces; fog has a smooth surface and is opaque owing to its optical thickness. The animated image facilitates effective classification because the fog is more static than the low-level cloud.

Another example is that of sea-ice images (Fig. 14). The GK2A RGB snow and fog image (right) represents snow and sea-ice in red. There is a large quantity of snow over land, and sea-ice is widespread over the Sea of Okhotsk (red area). This is also found in true-color imagery. Sea-ice has

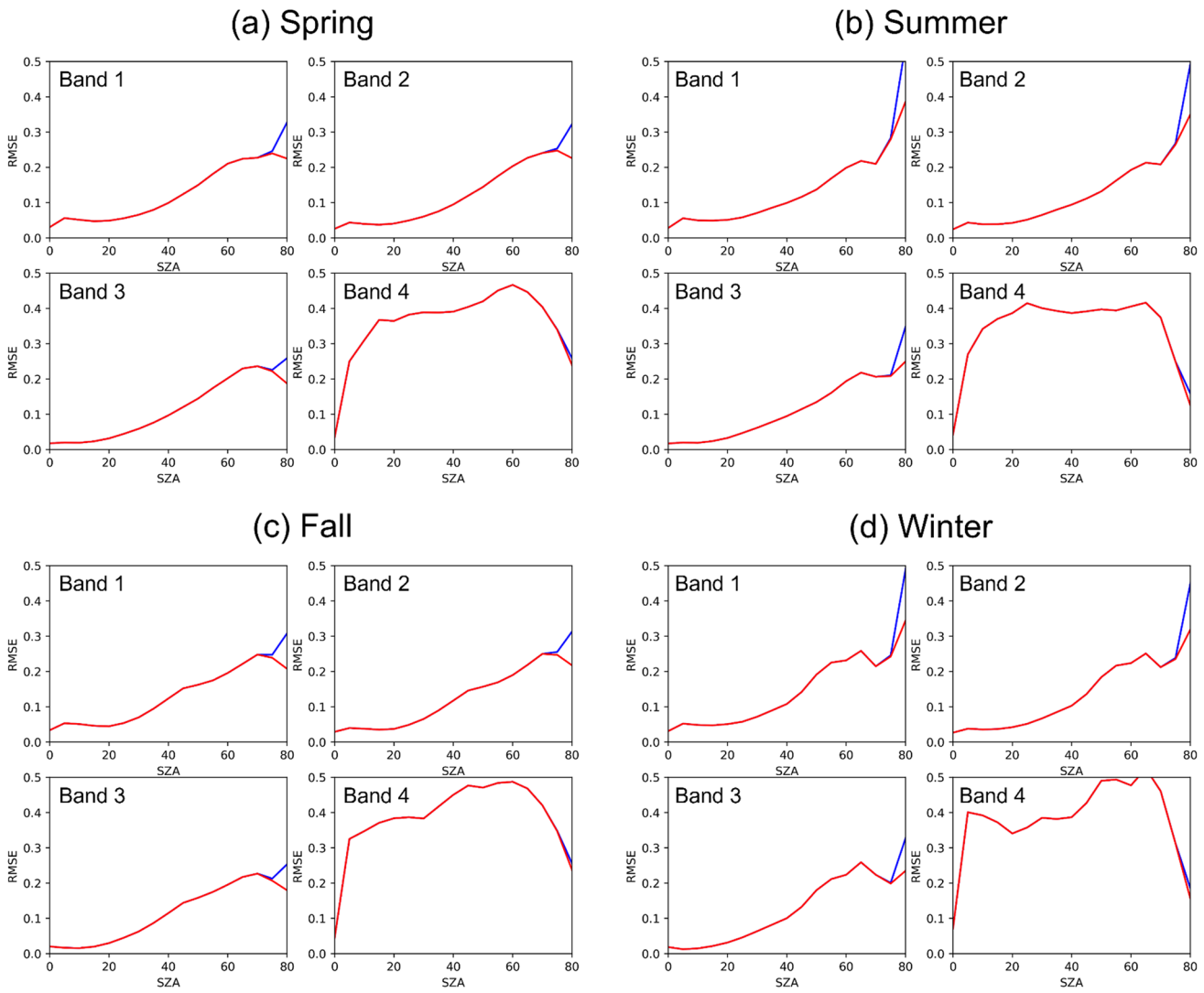

Fig. 11 Averaged RMSE of the difference between atmospheric corrected and blended reflectance on the original reflectance as a function of SZA for each band of (**a**) spring, (**b**) summer, (**c**) fall, and (**d**) winter season

the same color as cloud; however, it differs in terms of its shape and movements, sea-ice does not undergo changes of area coverage during the daytime.

Yellow dust is a weather phenomenon that occurs in desert areas in China and Mongolia, and in the middle Yellow River, where it is generated by strong winds or terrain and falls to the surface during long-distance transportation. The Fig. 15 shows the example of yellow dust in true-color imagery. The red box indicates yellow dust which represents as yellow and brown color and it travels with clouds. The Fig. 15 on the right is dust RGB from GK-2 A which shows yellow dust as red and hot pink color at the same time with true-color RGB imagery.

Figure 16 shows the typhoon MAYSAK (2020) in true-color imagery and enhanced color IR imagery from GK2A. Example of true-color imagery shows well-defined eyewall (red box) which is the most dangerous and destructive feature of typhoon and clear shape of convective structure. Right part of Fig. 16 also shows typhoon MAYSAK in enhanced color IR imagery. It highlights convective structure by repeating color and gray scale compared with traditional IR color scheme so in this figure, the structure of the typhoon and eyewall is more clearly separated.

4 Discussion

4.1 6S Parameterization for Building an LUT

The 6S uses sensitive RT code to predict a satellite signal at the satellite level for a Lambertian surface. Several parameters are required for it to make good estimations. However,

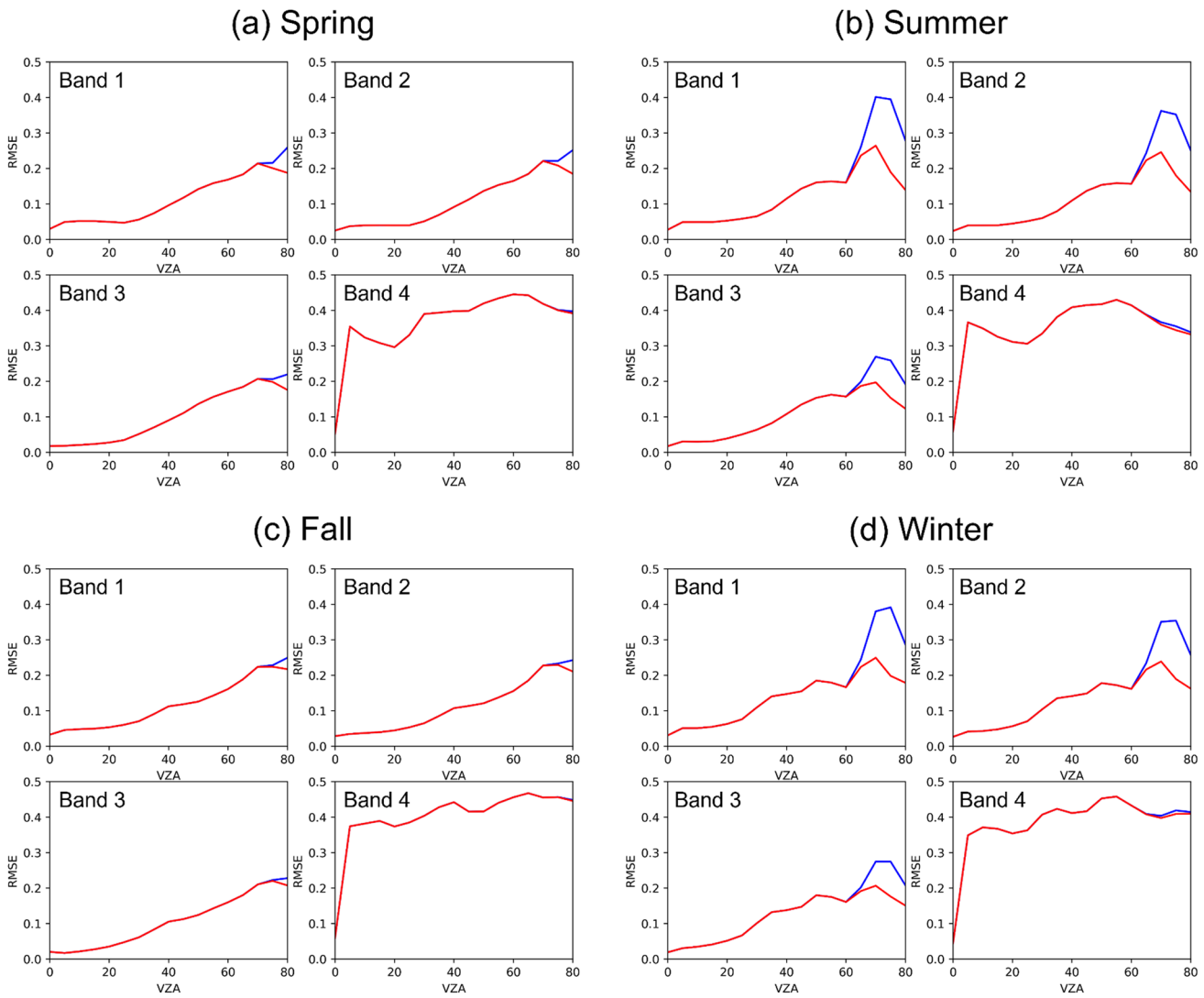

Fig. 12 Averaged RMSE of the difference between atmospheric corrected blended reflectance on the original reflectance as a function of VZA for each band of (**a**) spring, (**b**) summer, (**c**) fall, and (**d**) winter season

accurate model construction takes a lot of time; thus, a balance between simplicity and elaboration is required when setting the model configuration. Fortunately, the 6S model contains pre-prepared atmospheric conditions, which enable the specification of seasons (summer and winter), latitudinal zone (tropical, middle-latitude, and subarctic), the US standard atmosphere model (US62), and user-defined conditions; thus, it is possible to improve the model's ability without requiring the in-depth consideration of seasonality, the selection of a suitable molecular atmosphere model, or the frequent provision of input atmosphere data. During the process of atmospheric correction, an LUT that contains seasonally and latitudinally separated coefficients may give more accurate solutions. Furthermore, the conditions are sensitive to the aerosol model used; 6S sets "no aerosol" for simplicity and offers a number of land-type options (continental, maritime, urban, and desert). By implementing surface-type information, reflectance can be calculated using the coefficients derived from the LUT. Models differ through using different processes and atmospheric profiles. 6S calculates reflectance in terms of a bidirectional reflectance distribution function (BRDF) model. Numerous BRDF subroutines in 6S require a parameter for computing reflectance. Utilization of the 6SV2.1's detailed, in-built atmosphere models (which can more effectively address latitudinal and seasonal differences in the global atmosphere) can increase accuracy and may be implemented using the same LUT structure.

The computational costs involved in constructing an LUT introduces limitations to the design parameter conditions. One solution to this problem is to interpolate the LUT using an appropriate method, the MCS technique is one such validated method; it improves the quality of surface

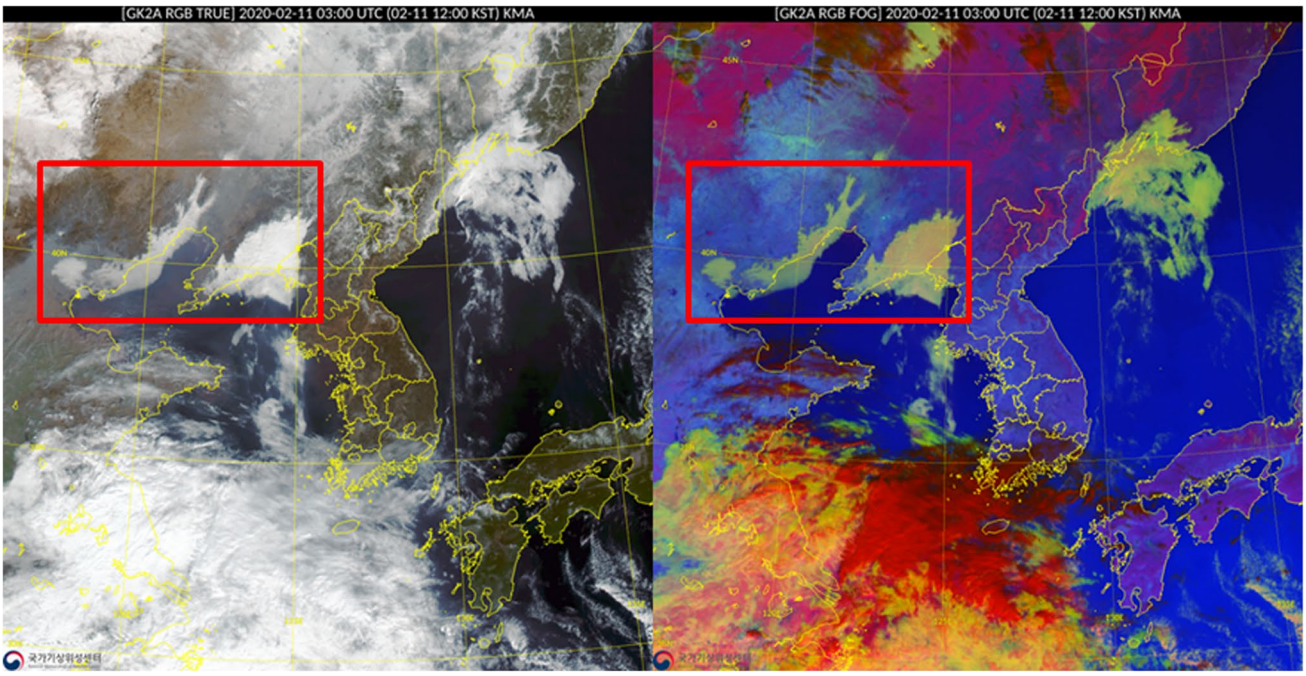

Fig. 13 Example of fog in the Korean Peninsula for true-color (left) and fog (right) RGB imagery, taken on 2020/02/11 0300 UTC

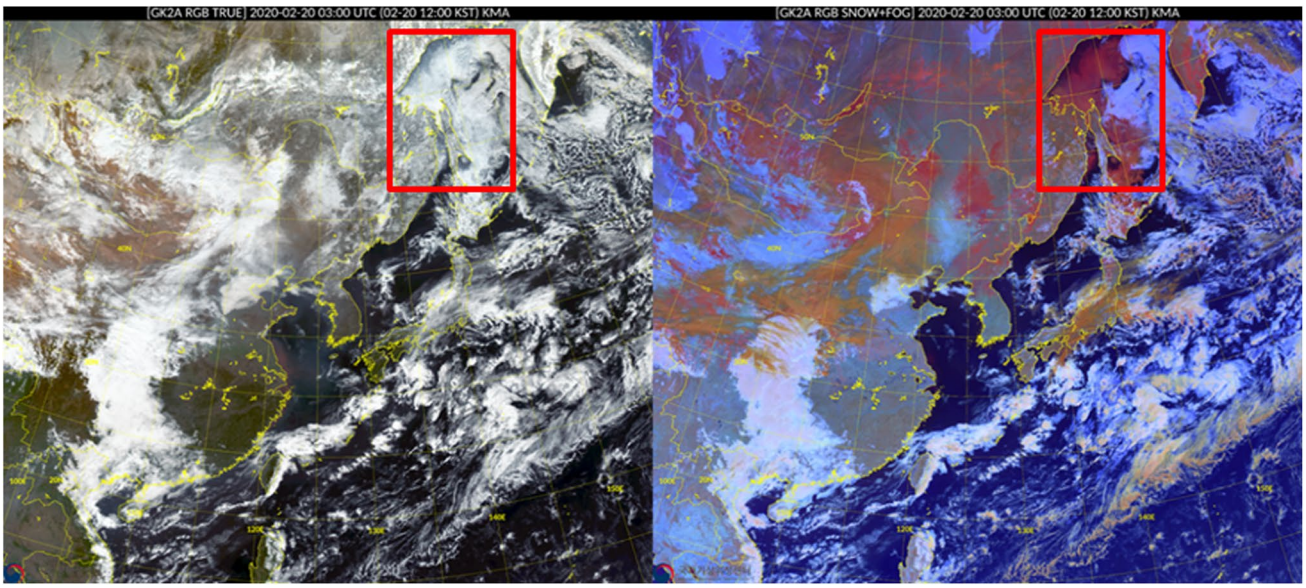

Fig. 14 Example of sea-ice in the East Asia for true-color (left) and day-snow-fog (right) RGB imagery, taken on 2020/02/20 0300 UTC

reflectance data, by interpolating the 6S LUT for application to the Himawari-8 AHI. Specifically, at high SZAs (greater than 75° SZA), improvements of 45.1 %, 39.6 %, 19.8 %, and 12.57 % in the relative root mean square errors were observed for Channels 1–4, respectively (Li et al. 2019). This method was here proposed for application to the GK2A AMI, and the results obtained were—when the atmospheric coefficients increased exponentially with the SZA and VZA—also consistent with those of the linearly interpolated method. The trends of the atmospheric coefficients also confirm that, for GK2A, xa is dependent only on the SZA, and xb is dependent on both the SZA and VZA (not shown); this corresponds with the results of Li et al. (2019) for Himawari-8 AHI.

Correction of the atmospheric distortion effects caused by molecular and particulate scattering and absorption is

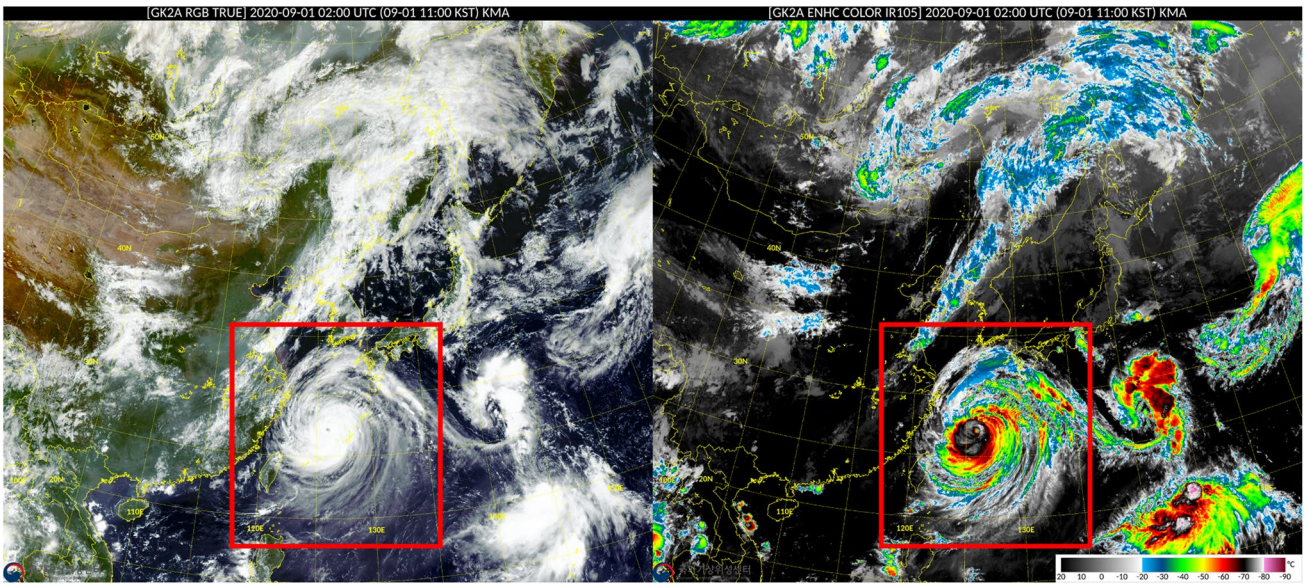

Fig. 15 Example of dust in the East Asia for true-color (left) and dust (right) RGB imagery, taken on 2021/03/15 0200 UTC

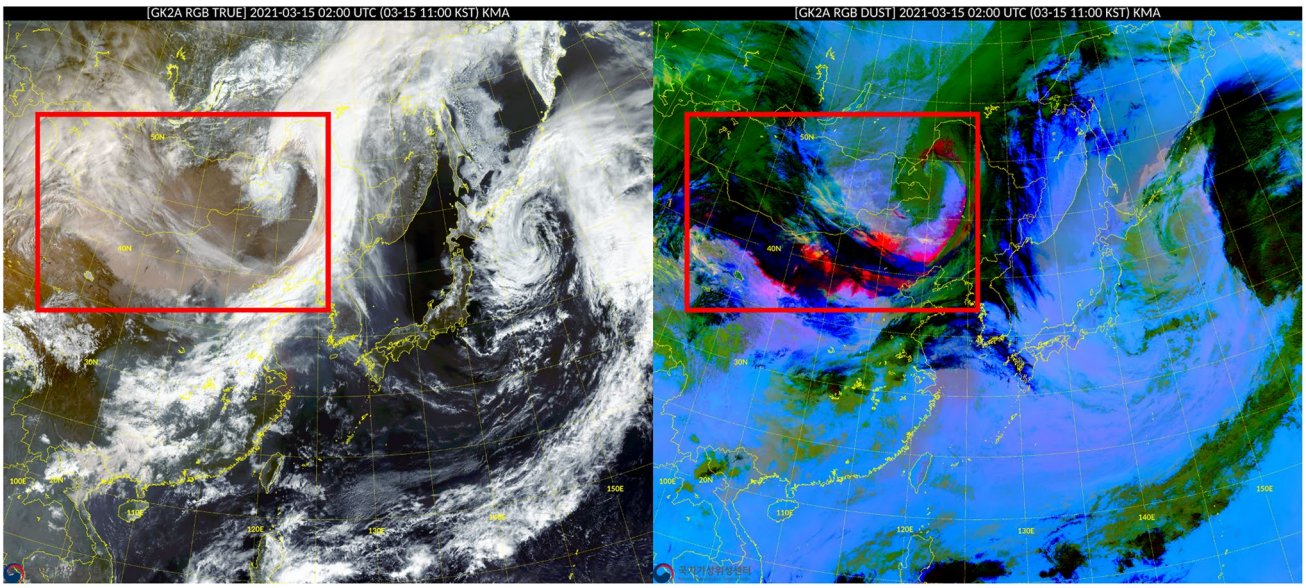

Fig. 16 Example of typhoon MAYSAK (2020) in East China Sea for true-color (left) and enhanced IR imagery (right), taken on 2020/09/01 0200 UTC

desirable whenever comparisons are to be made with data acquired under different atmospheric or geometric conditions. The absolute atmospheric correction of optical, remotely sensed data relies on RT codes. Several RT codes are available with different features; however, the most popular RT codes are 6S and MODTRAN. Callieco and Dell'Acqua (2011), compared two RT codes under identical geometric and atmospheric profile conditions. Their results showed that the mean relative difference between the simulated transmittances—obtained by subtracting the 6S transmittance from that of the MODTRAN—is small, at around 3.5 %. This is a result of the different assumptions used in calculating the light scattering process (Lee et al. 2020).

4.2 Limitation of 6S RTM

Earth has a spherical-shell atmosphere (SSA); however, almost all RT codes—including those of 6SV—are based on a parallel-plane atmosphere model, which assumes that

the Earth's surface and atmosphere are flat. In this case, RTMs tend to overcorrect the TOA reflectance above SZAs and VZAs of 70°; this issue is exacerbated when the two zenith angles approach one another. To resolve this problem, the Monte Carlo solver is an ideal approach, outperforming the SOS approximation (used in 6SV) or discrete ordinate (DISORT) code solver (used in MODTRAN, PSTAR, etc.); however, this method is not suitable for constructing an LUT because the computational cost is excessively high. Recently, an RT solver previously used in SOS and DISORT has been developed for improving the SSA model through pseudo-correction (Callieco and Dell'Acqua 2011; He et al. 2018). The atmospheric correction could succeed for high zenith angles, where the RT code alters the SSA structure model.

Some discussions remain around Rayleigh scattering at high zenith angles. This region contains very long optical paths, and high cloud can lead to further erroneous correction. The blending of Earth's limb regions entails the difficult task of discerning which region suffers the largest Rayleigh scattering effect. Broomhall et al. (2019) used a BT of 10.4 µm and alternatively applied another blending, instead of an uncorrected visible composite; this removed red edges and improved continuous nighttime scenes. Figure 17 shows an example of application of this method to GK2A. Although there is already a natural darkening around Earth's edge, brownish shadows may still appear in some regions where the SZA is large.

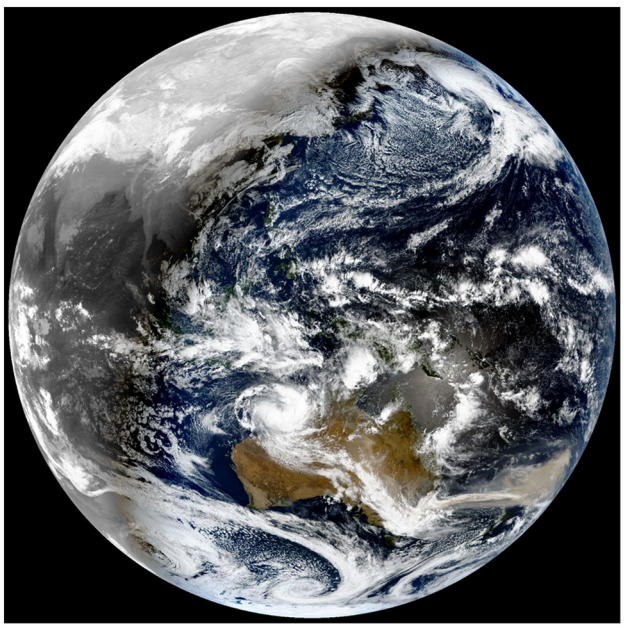

Fig. 17 Result of blending using a brightness temperature (BT) of 10.4 µm for GK2A. The visible imagery is blended with black at the limb, with the proportion varying linearly from 100–0 % for VZAs between 75° and 90° same date with Fig. 8

The solar radiation directly reflected by water surfaces is computed exactly using the Snell–Fresnel laws in the 6S; however, the sun-glint problems remain unresolved. System vicarious calibration (SVC) enables relative radiometric calibration to be achieved for satellite ocean color sensors. This could minimize uncertainty in the water-leaving radiance measured from TOA radiance and resolve the problems cause by sun glint (Zibordi et al. 2015).

4.3 Image Enhancement

At the extremities of SZA and VZA, data are blended for aesthetic reasons (Miller et al. 2016; Broomhall et al. 2019) applied this method—although in a slightly edited form—by moving the input-uncorrected RGB composite of the visible band into the infrared band. Overcorrected reflectance—which produces a red edge—can be blended with BT at the solar transition region. As exemplified by Broomhall et al. (2019), the blended imagery at high SZAs effectively removed the red edge along the Earth's limb. Figure 17 displays the result of blending using a BT of 10.4 µm for GK2A. The visible imagery is blended with black at the limb, with the proportion varying linearly from 100 to 0 % for VZAs between 75° and 90°.

This imagery technique has an additional advantage in that it provides visually continuous information during nighttime. The histogram equalization enhances color contrasts by redistributing the color histogram. The effect of histogram equalization is a distinctive brightening of the true-color images. However, the color distribution may be narrowed by the amount of light in the sample, such as during sunset or sunrise. Figure 18 shows a true-color scene at various times. The solar noon case shows Earth with a refined color distribution. As expected, it depicts ocean, land, cloud, and vegetation well. Images taken at other times—such as during sunrise and sunset—are low in brightness; in these, almost all features except clouds are shaded. The lower panels show the histograms of normalized reflectance—for pixel values between 0 and 255—before (dotted) and after (line) applying histogram equalization. The shape of the histogram before equalization in the solar noon case differs from the others, which exhibit wider distributions. After histogram equalization was applied, their shape became very similar. This suggests that corrective color redistribution may be possible; however, the input dataset has a low performance in discriminating subtle differences in the reflecting surface type.

5 Conclusions

This paper described the production of atmospherically corrected, true-color GK2A RGB imagery. The main process is separated into absolute atmospheric correction and relative

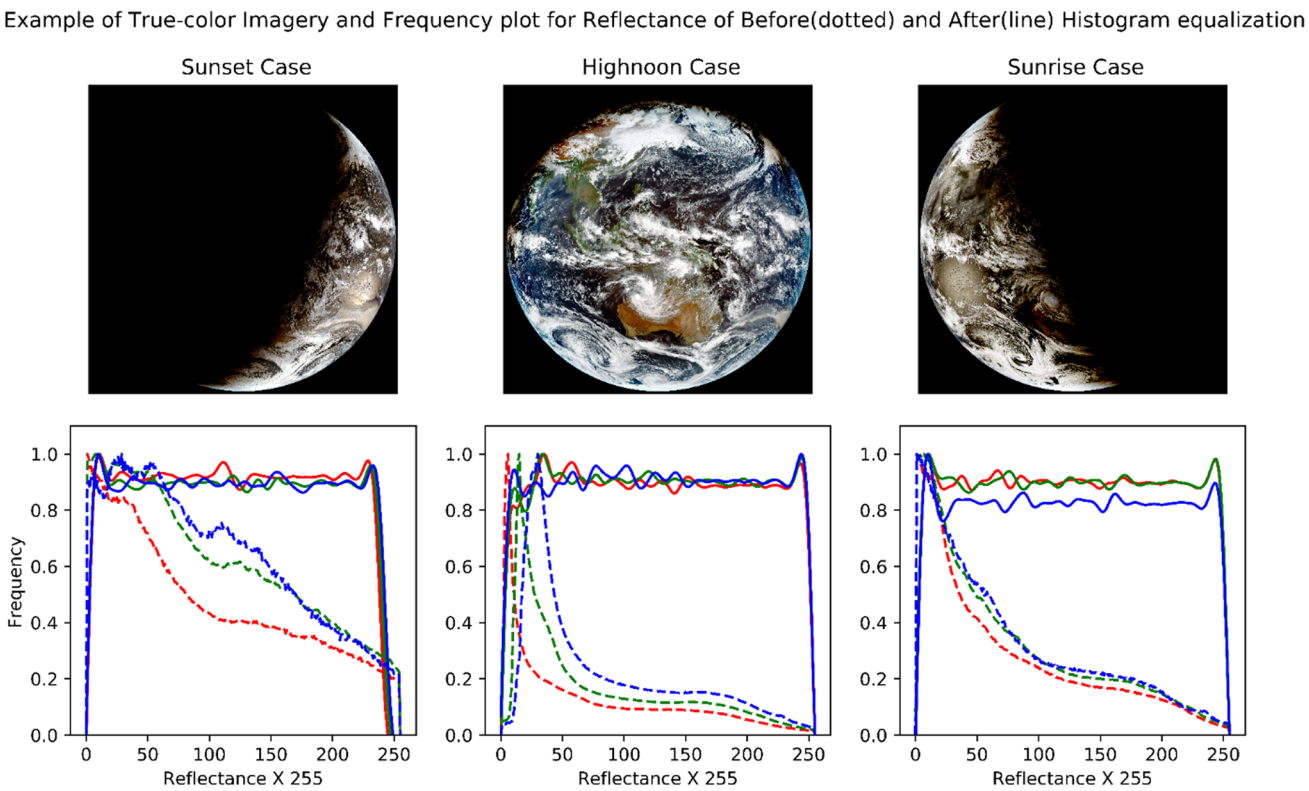

Fig. 18 Example of true-color imagery and frequency plot of reflectance before (dotted) and after (line) histogram equalization

atmospheric correction, based on image-processing techniques. LUTs represent a practical approach to performing atmospheric corrections that require the processing of large quantities of data (GK2A produces 22,000 × 22,000 and 11,000 × 11,000 pixel scenes of 0.5 and 1 km resolutions every 10 min, respectively).

To generate true-color imagery, all datasets must have an identical spatial resolution; thus, the visible (excluding the 640 nm band), vegetation, and infrared channels were downscaled to 500 m (the spatial resolution of the 640 nm band—the sharpest channel). During statistical downscaling, spline interpolation was used to sharpen resolution. An LUT was built considering the geometric parameters (SZA, VZA, and RAA), atmospheric parameters (TCO, TPW, and AOD), and reflectance height from the ground (up to 10 km). The three pre-calculated atmospheric correction coefficients were stored in the LUT. To augment the LUT, an MCS technique was applied.

The RTM can be extended to distinguish cloud-top heights. In this case, the pathlength is described for each pixel, which avoids the requirement for pathlength correction during the atmospheric correction process. These enhancements have the potential to improve the accuracy of the Rayleigh-corrected reflectance, particularly at higher SZAs and VZAs. Adding the RTM's capacity to perform Rayleigh corrections with defined pathlengths would require an appropriate elevation model and cloud-height product; thus, many more RT computations would need to be performed (a unique set for each selected pathlength), and an extra dimension would be required in the LUT structure. It is unlikely that the visible appearance of the true-color imagery would be significantly improved by including pathlength as an extra variable in the atmospheric correction process, except perhaps for the highest VZAs and SZAs. To quantitatively confirm the effect of atmospheric correction, RMSE was analyzed in accordance with SZA and VZA and found to be in the range of 0–0.5. As SZA increases, the effect of atmospheric scattering is enhanced and the RMSE due to atmospheric correction increases. In particular, RMSE increases significantly as it exceeds 70 degrees. As the scattering is stronger as it goes to the shorter band, the improvement of the reflectivity is noticeable.

Each original band that composes a true-color image has a different spatial resolution. To match the resolutions, spline interpolation was used. Downscaled imagery is expected to express coastlines and cloud surfaces in detail. Utilizing the methods of Miller et al. (2016), it is possible to produce a hybrid green band that better matches the peak reflectance of chlorophyll (~555 nm). The initial atmospherically corrected true-color RGB images contained large, unrealistic values for long atmospheric pathlengths near Earth's limb, owing to overcorrection by the 6S RTM (Miller et al. 2016).

One method of overcoming this difficulty is to blend the atmospherically corrected true-color RGB imagery with uncorrected imagery near the limb. It was found that the quantitative improvement of the reflectivity according to the blending technique increased the correction effect according to the cloud height as the VZA increased.

Even after atmospheric correction, true-color imagery appeared dark and lacked contrast. Histogram equalization, which adjusts the brightness and contrast of images by redistributing the histogram of the RGB composite, was used to produce vivid true-color images. True-color information provides a practical method for interpreting a wide variety of environmental phenomena. High-temporal-resolution true-color imagery from the GK2A AMI provides a tool for scientists and forecasters to visualize the changing Earth and has considerable potential to engage the general public in an intuitive manner. We anticipate that our procedure, with its successful integration of a number of sub-processes pertaining to the GK2A AMI, will constitute a significant step in this direction.

Authors' Contributions Minsang Kim conceived and designed the experiments; Minsang Kim performed the experiments; Minsang Kim, Jun-Hyung Heo, and Eun-Ha Sohn analyzed the data; Minsang Kim, Jun-Hyung Heo, and Eun-Ha Sohn contributed materials and analysis tools; Minsang Kim and Jun-Hyung Heo wrote the paper; Eun-Ha Sohn managed the whole process of the research.

Funding This work was funded by the Korea Meteorological Administration's Research and Development Program "Technical Development on Weather Forecast Support and Convergence Service using Meteorological Satellites" under Grant (KMA2020-00120).

Data Availability Not applicable.

Code Availability Not applicable.

Declarations

Conflicts of Interest/Competing Interests The authors declare no conflict of interest.

References

Adler-Golden, S.M., Matthew, M.W., Bernstein, L.S., Levine, R.Y., Berk, A., Richtsmeier, S.C., Acharya, P.K., et al.: Atmospheric correction for shortwave spectral imagery based on Modtran4. Proc. SPIE 3753 Imaging Spectrometry V: 61–69 (1999). https://doi.org/10.1117/12.366315

Agust-Panareda, A, Massart, S, Chevallier, F, Boussetta, S, Balsamo, G, Beljaars, A: Forecasting global atmospheric CO 2. Atmos. Chem. Phys. **14**(21), 11959–11983 (2014). https://doi.org/10.5194/acp-14-11959-2014

Bah, M.K., Gunshor, M.M., Schmit, T.J.: Generation of GOES-16 true color imagery without a green band. Earth Space Sci. **5**(9), 549–558 (2018). https://doi.org/10.1029/2018EA000379

Berka, A., Anderson, G.P., Bernstein, L.S., Acharya, P.K., Dothe, H., Matthew, M.W., Adler-Golden, S.M., et al.: MODTRAN4 radiative transfer modeling for atmospheric correction. Optical spectroscopic techniques and instrumentation for atmospheric and space research III. International Society for Optics and Photonics, 3756, pp. 348–353 (1999)

Bessho, K., et al.: An introduction to Himawari-8/9—Japan's new-generation geostationary meteorological satellites. J. Meteor. Soc Jpn. **94**(2), 151–183 (2016). https://doi.org/10.2151/jmsj.2016-009

Broomhall, M.A., Majewski, L.J., Villani, V.O., Grant, I.F., Miller, S.D.: Correcting Himawari-8 advanced himawari imager data for the production of vivid true-color imagery. J. Atmos. Ocean. Technol. **36**(3), 427–442 (2019)

Callieco, F., Dell'Acqua, F.: A comparison between two radiative transfer models for atmospheric correction over a wide range of wavelengths. Int. J. Remote Sens. **32**(5), 1357–1370 (2011)

Csiszar, I., Gutman, G.: Mapping global land surface albedo from NOAA AHVRR. J. Geophys. Res-Atmos. **104**(D6), 6215–6228 (1999). https://doi.org/10.1029/1998JD200090

Dorji, P., Fearns, P.: Atmospheric correction of geostationary Himawari-8 satellite data for total suspended sediment mapping: a case study in the coastal waters of Western Australia. ISPRS J. Photogramm. Remote Sens. **144**, 81–93 (2018). https://doi.org/10.1016/j.isprsjprs.2018.06.019

Engelen, R.J., McNally, A.P.: Estimating atmospheric CO 2 from advanced infrared satellite radiances within an operational four-dimensional variational (4d-Var) data assimilation system: results and validation. J. Geophys. Res. **110**, 18305 (2005). https://doi.org/10.1029/2005JD005982

Franch, B., Vermote, E.F., Sobrino, J.A., Fédèle, E.: Analysis of directional effects on atmospheric correction. Remote Sens. Environ. **128**, 276–288 (2013)

Fukushima, H., Higurashi, A., Mitomi, Y., Nakajima, T., Noguchi, T., Tanaka, T., Toratani, M.: Correction of atmospheric effect on ADEOS/OCTS ocean color data: algorithm description and evaluation of its performance. J. Oceanogr. **54**(5), 417–430 (1998)

Geiger, B., Carrer, D., Franchisteguy, L., Roujean, J.-L., Meurey, C.: Land surface albedo derived on a daily basis from Meteosat second generation observations. IEEE Trans. Geosci. Remote Sens. **46**(11), 3841–3856 (2008). https://doi.org/10.1109/TGRS.2008.2001798

Ghulam, A., Qin, Q., Zhu, L.: 6S model-based atmospheric correction of visible and near-infrared data and sensitivity analysis. Acta Sci. Nat. Univ. Pekin. **40**, 611–618 (2004)

Gordon, H.R.: Radiative transfer in the atmosphere for correction of ocean color remote sensors. In Ocean Colour: Theory and applications in a decade of CZCS experience, edited by Barale V. and Schlittenhardt P.M. Eurocourses: Remote Sens. **3**, 33–77 (1993)

He, T., Zhang, Y., Liang, S., Yu, Y., Wang, D.: Developing land surface directional reflectance and albedo products from geostationary GOES-R and Himawari data: theoretical basis, operational

implementation, and validation introducing the next generation advanced baseline imager on GOES-R. Remote Sens. **11**(22), 2655 (2019)
He, X., Stamnes, K., Bai, Y., Li, W., Wang, D.: Effects of earth curvature on atmospheric correction for ocean color remote sensing. Remote Sens. Environ. **209**, 118–133 (2018)
Inness, A., Ades, M., Agust-Panareda, A., Barré, J., Benedictow, A., Blechschmidt, A.-M.: The CAMS re-analysis of atmospheric composition. Atmos. Chem. Phys. **19**(6), 3515–3556 (2019). https://doi.org/10.5194/acp-19-3515-2019
Karpouzli, E., Malthus, T.: The empirical line method for the atmospheric correction of IKONOS imagery. Int. J. Remote Sens. **24**(5), 1143–1150 (2003)
Kim, D., Gu, M., Oh, T.H., Kim, E.K., Yang, H.J.: Introduction of the advanced meteorological imager of Geo-Kompsat-2a: In-orbit tests and performance validation. Remote Sens. **13**(7), 1303 (2021). https://doi.org/10.3390/rs13071303
Lee, C.S., Yeom, J.M., Lee, H.L., Kim, J.J., Han, K.S.: Sensitivity analysis of 6S-based look-up table for surface reflectance retrieval. Asia-Pac. J. Atmos. Sci. **51**, 91–101 (2015). https://doi.org/10.1007/s13143-015-0062-9
Lee, K.S., Lee, C.S., Seo, M., Choi, S., Seong, N.H., Jin, D., Yeom, J.M., Han, K.S.: Improvements of 6S look-up-table based surface reflectance employing minimum curvature surface method. Asia-Pac. J. Atmos. Sci. **56**, 1–14 (2020). https://doi.org/10.1007/s13143-019-00164-3
Li, H., He, X., Shanmugam, P., Bai, Y., Wang, D., Huang, H.: Radiometric sensitivity and signal detectability of ocean color satellite sensor under high solar zenith angles. IEEE Trans. Geosci. Remote Sens. **57**(11), 8492–8505 (2019)
Liang, S., Fang, H., Chen, M.: Atmospheric correction of landsat ETM + land surface imagery. I. methods. IEEE Trans. Geosci. Remote Sens. **39**, 2490–2498 (2001). https://doi.org/10.1109/36.964986
Lyapustin, A., Martonchik, J., Wang, Y., Laszlo, I., Korkin, S.: Multi-angle implementation of atmospheric correction (MAIAC): 1. Radiative transfer basis and look-up tables. J. Geophys. Res. Atmos. **116**, 3 (2011). https://doi.org/10.1029/2010JD014986
Massart, S., Agustí-Panareda, A., Heymann, J., Buchwitz, M., Chevallier, F., Reuter, M.: Ability of the 4-D-var analysis of the GOSAT BESD XCO 2 retrievals to characterize atmospheric CO 2 at large and synoptic scales. Atmos. Chem. Phys. **16**(3), 1653–1671 (2016). https://doi.org/10.5194/acp-16-1653-2016
Miller, S.D., Schmit, T.L., Seaman, C.J., Lindsey, D.T., Gunshor, M.M., Kohrs, R.A., Sumida, Y., Hillger, D.: A sight for sore eyes: the return of true color to geostationary satellites. Bull. Am. Meteorol. Soc. **97**(10), 1803–1816 (2016)
Proud, S.R., Fensholt, R., Rasmussen, M.O., Sandholt, I.: (2010). A comparison of the effectiveness of 6S and SMAC in correcting for atmospheric interference of Meteosat Second Generation images. J. Geophys. Res. Atmos. **115**(D17)
Qu, Z., Kindel, B.C., Goetz, A.F.: The high accuracy atmospheric correction for hyperspectral data (HATCH) model. IEEE Trans. Geosci. Remote Sens. **41**(6), 1223–1231 (2003)
Rabah, M, Kaloop, M: The use of minimum curvature surface technique in geoid computation processing of Egypt. Arab. J. Geosci. **6**(4), 1263–1272 (2013)
Rahman, H., Dedieu, G.: SMAC: a simplified method for the atmospheric correction of satellite measurements in the solar spectrum. Remote Sens. **15**(1), 123–143 (1994)
Richter, R.: Atmospheric correction of DAIS hyperspectral image data. Comput. Geosci. **22**(7), 785–793 (1996)
Richter, R., Schlapfer, D., Muller, A.: An automatic atmospheric correction algorithm for visible/NIR imagery. Int. J. Remote Sens. **27**(10), 2077–2085 (2006)
Ruddick, K., Neukermans, G., Vanhellemont, Q., Jolivet, D.: Challenges and opportunities for geostationary ocean colour remote sensing of regional seas: a review of recent results. Remote Sens. Environ. **146**, 63–76 (2014). https://doi.org/10.1016/j.rse.2013.07.039
Schaaf, C.B., Gao, F., Strahler, A.H., Lucht, W., Li, X., Tsang, T., Strugnell, N.C.: First operational BRDF, albedo and nadir reflectance products from MODIS. Remote Sens. Environ. **83**(1–2), 135–148 (2002). https://doi.org/10.1016/S0034-4257(02)00091-3
Schmit, T., Griffith, P., Gunshor, M., Daniels, J., Goodman, S., Lebair, W.: A closer look at the ABI on the GOES-R series. Bull. Amer. Meteor. Soc. **98**(4), 681–698 (2016). https://doi.org/10.1175/BAMS-D-15-00230.1
Smith, W.H.F., Wessel, P.: Gridding with continuous curvature splines in tension. Geophys **55**, 293–305 (1990)
Sriwongsitanon, N., Surakit, K., Thianpopirug, S.: Influence of atmospheric correction and number of sampling points on the accuracy of water clarity assessment using remote sensing application. J. Hydrol. **401**(3–4), 203–220 (2011)
Strugnell, N.C., Lucht, W.: An algorithm to infer continental-scale albedo from AVHRR data, land cover class, and field observations of typical BRDFs. J. Clim. **14**(7), 1360–1376 (2001). https://doi.org/10.1175/1520-0442(2001)014
Vermote, E., Tanre, D., Deuze, J.L., Herman, M., Morcette, J.-J.: Second simulation of the satellite signal in the Solar Spectrum-Vector (6SV): an overview. IEEE Transact. Geosci. Remote Sens. **35**, 675–686 (2006)
Wang, M.: Rayleigh radiance computations for satellite remote sensing: accounting for the effect of sensor spectral response function. Opt. Express **24**, 12414–12429 (2016). https://doi.org/10.1364/OE.24.012414
Yang, J, Zhang, Z, Wei, C, Lu, F, Guo, Q: Introducing the new generation of Chinese geostationary weather satellites, Fengyun-4. Bull. Am. Meteor. Soc. **98**(8), 1637–1658 (2017). https://doi.org/10.1175/BAMS-D-16-0065.1
Zhou, J., Wang, J., Li, J., Hu, D.: Atmospheric correction of PROBA/CHRIS data in an urban environment. Int. J. Remote Sens. **32**(9), 2591–2604 (2011). https://doi.org/10.1080/01431161003698443
Zibordi, G, Melin, F, Voss, KJ, Johnson, BC, Franz, BA, Kwiatkowska, E: System vicarious calibration for ocean color climate change applications: Requirements for in situ data. Remote Sens. Environ. **159**, 361–369 (2015)